Hindawi
Advances in Civil Engineering
Volume 2021, Article ID 6637754, 20 pages
https://doi.org/10.1155/2021/6637754

Research Article

Seismic Optimization of High Cantilever Multianchor Pile Strengthening Soil Slopes against Earthquakes

Honggang Wu,[1] Lifang Pai,[1,2] and Hao Lei[1]

[1]*Northwest Research Institute Co., Ltd of C.R.E.C, Lanzhou, Gansu 730000, China*
[2]*China Academy of Railway Sciences, Beijing 100081, China*

Correspondence should be addressed to Lifang Pai; 1072191799@qq.com

Received 19 October 2020; Revised 5 December 2020; Accepted 17 December 2020; Published 30 January 2021

Academic Editor: Chong Xu

To explore the optimal seismic performance of multianchor pile, we carried out a series of shaking table tests. Based on the special form of multianchor piles' reinforcement, we put forward the optimal design scheme of using EPS foam as damping layers and energy-dissipation springs for improving the self-coordinating devices of anchor head. By measuring acceleration and dynamic soil-pressure response under different intensities of vibration, we analyzed the correlation between acceleration caused by seismic wave action and damage characterized by time-domain and spectral characteristics of dynamic soil-pressure. We discuss in detail the relationship between frequency and specific period of dynamic soil-pressure and acceleration. We then used the SPECTR program to calculate the energy spectrum. Under the reciprocating action of seismic waves of different intensities, our slope model showed the continuous effect of spatial coupling deformation leading to regional damage and failure. Furthermore, the spatial distribution for amplitude of acceleration and dynamic soil-pressure showed the outstanding response of lateral amplitude of pile structures without optimization. The energy-spectrum distribution of acceleration seismic input was orderly, while the dynamic soil-pressure distribution of piles was disordered. Low-frequency (≤10 Hz) seismic waves have a great influence on these structures. The difference of acceleration hysteresis along the elevations was mainly caused by the propagation stage after the main earthquake. The correlation between dynamic soil-pressure and acceleration response in each group before the pile occurred in the same earthquake area was very weak, showing a low correlation. The optimization effect of optimized structures is related to the position of the shock-absorbing layer. Under high acceleration, multianchor piles easily cause bulge failures or shear failures at the positions of sliding surfaces. These results are helpful for improvements to reliably optimize designs in pile structure dynamic parameters.

1. Introduction

Current plate-tectonic theory describes seismic activity in terms of high frequency, high intensity, shallow source, and wide distribution. Earthquakes and other natural disasters have become one of the great challenges that must be addressed globally [1]. China is located between the two famous seismic belts of the Pacific Rim and Europe and Asia. A large number of high filling and deep excavation slopes and natural mountain slopes in highway and railway traffic projects are scattered along moderate and strong earthquakes. The slope instability induced by earthquakes has become one of the typical causes of accidents in geotechnical engineering. Considering economy and rationality of design, pile-anchor retaining structures have become the safest, most reliable designs, while their performance was directly affected in the event of an earthquake. They enhance the stability of a slope's reinforcement but often become weak alone the seismic zones of fault lines. Once a problem occurs, the consequences will be incalculable [2].

Recent research on pile-anchor retaining structures during earthquakes has focused mainly on theoretical and numerical calculations, prototype investigations, and model tests. The objects of this research have included seismic response characteristics of structures and slopes, mechanisms of failure with earthquake damage, and other dynamic characteristics.

The dynamic response of retaining structures in antislide piles has been studied mainly through theoretical analysis, numerical calculation, shaking table tests, and centrifuge tests. Such studies focus on the dynamic interaction between structures and their rock soil media. Zhang and Wolf [3] and Fang [4] carried out multiple theoretical analyses concerning the dynamic interactions of soil-pile systems, thus enriching basic theory in this field. Maheshwari et al. [5] and Takewaki and Kishida [6] used numerical-analytic software to calculate dynamic interactions of soil-pile systems under earthquake conditions, pointing out the characteristic seismic responses in different modes by single pile and group pile. Ye et al. [7] and Lai et al. [8] carried out a large number of vibration tests and centrifuge tests on the support forms of single-row and double-row antislide piles. They revealed the failure mechanism in earthquake damage under various intensity earthquake effects. They also provided a basis for seismically optimal design of slopes in high-intensity areas.

Single-anchor antislide piles using prestressed anchor cable were developed in the 1980s and used widely in China and in other nations for landslide remediation engineering [9]. However, calculation methods and design principles for such piles currently have no clear regulations or guidelines, especially when it comes to dynamic response during earthquakes. The theoretical research cannot keep up with the pace of engineering applications, and in-depth research remains to be done [10]. At present, research on prestressed anchor-cable antislide piles focuses mainly on model tests, numerical calculations, and optimal design. Zhang [8] and Liu et al. [11] analyzed the stress and deformation of piles based on different assumptions and calculation theories, but they ignored the joint effect of the deformation of piles and anchor cables. Fan et al. [12]; Bi et al. [13]; and Zou et al. [14] used vibration-table design model tests to reveal quantified response laws of landslide acceleration, antislide pile bending moments, dynamic pressure between pile and soil, and anchor-cable axial force at different peak values of earthquake action. Martin and Chen [15]; Huang et al. [16]; and other scholars used finite-difference FLAC3D software to construct a slope model for prestressed anchor-cable antislide pile reinforcements. They observed slope surface displacement, peak acceleration amplification factor of slope surfaces, and stress on supporting structures in earthquakes.

There is little engineering experience of antislide piles using multianchor prestressed anchor cable (to which we will refer using the term multianchor piles). Internationally, there is virtually no information on multianchor piles. Such piles were first proposed and used in the large-scale, complex landslide treatment project at Jietai Temple, Beijing [17]. Deng [18] and Wang [19] first carried out theoretical analysis for relevant statics, as well as numerical calculation of the stress and deformation in multianchor piles. They provided a foundation for research in reducing stress and displacement of pile bodies and in optimizing the spacing between anchor points. Ai [20] and Feng et al. [21] carried out preliminary explore action of acceleration-dynamic response in multianchor piles using a shaking table test and obtained a distribution of peak acceleration along pile bodies.

In view of the complexity of response characteristics in soil-pile systems' wave propagation interactions across various media, we still have a poor understanding of dynamic load characteristics with acceleration and dynamic soil-pressure changes under seismic action. In some cases, seismic design for reinforced slopes remains largely based on engineering experience. In addition, since antislip structures on reinforced slopes must undergo large deformations or displacements during strong earthquakes, it is necessary to clarify characteristics of distribution and variation in acceleration and dynamic soil-pressure under various earthquake intensities.

Therefore, we aimed to study dynamic soil-pressure and acceleration dynamic response's spatial variations, in soil slopes strengthened using multianchor piles under earthquake conditions. Based on the special form of multianchor piles' reinforcement, we put forward the optimal design scheme of using EPS foam as damping layers and energy-dissipation springs for improving the self-coordinating devices of anchor head. In this research, we have carried out a series of shaking table tests. We examined (1) time-domain characteristics of deformation, acceleration, and dynamic soil-pressure in slope models under seismic action of various intensities, obtaining regional spatial distribution characteristics of slope reinforcement effects along pile elevations at different positions with multiple anchor points. Based on Fourier change and statistical probability scatter matrix operations, we discuss (2) details of correlations between pile acceleration and dynamic soil-pressure response-spectrum characteristics in reinforced slopes under seismic action. We compared (3) the relationship of frequency to specific period, by acceleration and dynamic soil-pressure, at different vibration stages. We then used the SPECTR program to further discuss (4) energy transmutation in ground-motion damage and deformation failure.

2. Shaking Table Test Setup

2.1. Overview of Vibration Table. The shaking table tests were carried out using the servo-driven seismic simulation shaking table at the Lanzhou Institute of Seismology, China Seismological Bureau. This shaking table has its own 64-channel dynamic data acquisition system, which can realize horizontal and vertical two-way vibration loading. The main technical parameters are shown in Table 1 [22].

In many cases, failures occur on slopes with potential sliders, mainly limited to the upper part and both sides of a slope. In this case, possible upward or transverse motion (perpendicular to the main sliding direction) can be limited [23]. To check the dynamic response of this soil slope, we used a rigid model box. The vibration table was therefore equipped with a rigid model box with dimensions of 3.00 m × 1.40 m × 1.14 m (length × width × height), as shown in Figure 1. Inside the rigid model box, two sides were made of plexiglass while the side perpendicular to the direction of horizontal excitation was steel plate. The model box, a commonly used device for studies of dynamic characteristics in soil structure using shaking table tests, was fixed on the table by bolts connected rigidly around it [22].

Table 1: Technical parameters of the shaking table test system.

Parameters	Technical specification
Table size	4 m × 6 m
Mode of motion	Horizontal one-way, vertical one-way, horizontal and vertical coupling
Input waveform	Regular wave, random wave, seismic wave, artificial wave
Maximum bearing capacity	*X*, *Z* (single vibration): *X*, 20 *t*; Z, 15 t *X*, *Z* (combined vibration): *X*, 15 *t*; Z, 15 t
Maximum displacement	*X*, *Z* (single vibration): *X*, ±250 mm; *Z*, ±100 mm *X*, *Z* (combined vibration): *X*, ±150 mm; *Z*, ±100 mm
Maximum velocity	*X*, *Z* (single vibration): *X*, 1500 mm/s; *Z*, 700 mm/s *X*, *Z* (combined vibration): *X*, 1000 mm/s; *Z*, 700 mm/s
Maximum acceleration	*X*, *Z* (single vibration): *X*, 1.7 g; *Z*, 1.2 g *X*, *Z* (combined vibration): *X*, 1.2 g; *Z*, 1.0 g
Range of operating frequency	*X*, *Z* (single vibration): *X*, 0.1–70 Hz; *Z*, 0.1–50 Hz *X*, *Z* (combined vibration): *X*, 0.1–50 Hz; *Z*, 0.1–50 Hz

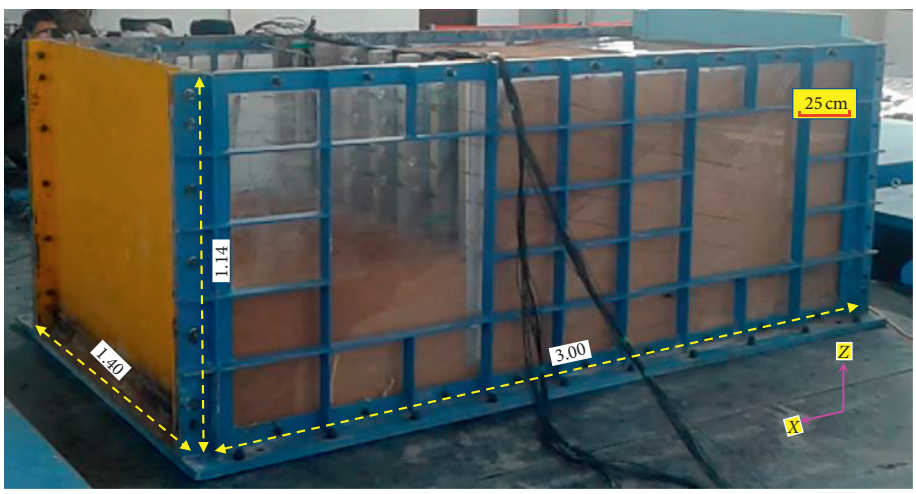

Figure 1: Shaking table and model box (unit: m).

Considering the influence of rigid model box boundary effect, the model box boundary needed to be processed [24]. The boundary of the model box perpendicular to the horizontal excitation can form shock reflection, altering the wave transmission considerably. We pasted polystyrene foam plastic board (5 cm thick) to the inner wall, treating the boundary of the model box perpendicular to the direction of horizontal excitation as a flexible boundary [25]. To reduce contact friction between the model and the boxes with two inner side walls, we applied a layer of Vaseline to the inner surface of the plexiglass on two inner side of the box and processed the sliding boundary on two inner sides [26]. Because seismic waves were input from the bottom of the model box, there was no relative sliding between the model's soil and the bottom of the box. To ensure good adhesion, we increased friction by placing a layer of gravel soil (5 cm thick) on the bottom of the model box. The gravel diameter was about 2 cm, and the bottom plate was treated as a friction boundary [27].

2.2. Optimization of Multianchor Pile Design. The multianchor pile was optimized to be a rigid and flexible composite structure, mainly including a reinforced concrete pile, an EPS foam and wall protection, anchor cable, an energy-dissipation spring, and an anchor tool. The design and implementation methods for the structure were as follows.

First, the pile pit for the reinforced concrete pile was excavated section by section and a retaining wall was applied for each section in time until the pile pit was excavated for the design elevation. Then, the EPS foam's precast blocks were installed, from the bottom of the pile pit to the top, section by section. The thickness of these blocks was no less than 50 cm and the height was 3–5 m. We joined the precast blocks of EPS foam with the retaining wall by setting two reserved rebars at the top of each section of the retaining wall. During installation, these rebars were inserted into their reserved holes in the precast blocks of EPS foam, and each block was bonded to the retaining wall using adhesive so as to avoid contact between the surface of blocks and the retaining wall's joints.

We next bound the reinforcement cage, pouring and curing reinforced concrete for the antislide pile. The anchor cable, reserved pipe, and steel cage were installed synchronously, and the reinforced concrete pile was poured onsite. The retaining wall and EPS foam's precast block were connected by joining the reserved holes in the EPS to matching reinforcements on the retaining wall. The EPS

foam's precast block and retaining wall were bonded using adhesive. Finally, when the antislide pile reached 85% of the designed strength, the prestressed anchor cable was installed. We found out the reserved position of the antislide pile-anchor cable, removed the soil from the front as well as the protective wall at that point, and found the reserved hole for the anchor cable. Installing the cable and grouting, as well as the energy-dissipation spring at the anchor head for each external anchor section, we tense-sealed the anchor. A flowchart for the process is shown in Figure 2.

The optimized multianchor pile organically combined the three rigid and flexible materials of the reinforced concrete structure, EPS foam, and energy-dissipation spring. An EPS foam was arranged on the side of the pile to reduce the dynamic response of the structure. The energy-dissipation spring self-coordinating device was set between the anchor head and the pile, playing a buffering role and improving the stress condition of the anchor head by stretching and deforming the spring. This not only met the requirements for landslide resistance thrust but also improved the seismic performance of the structure, showing a broad practical prospect for areas with high seismic intensity.

2.3. Test Model Setting. This test did not target the given engineering prototype, but we considered the size of the shaking table model box and the possible application of this model in actual construction projects. For a practical project, we adopted similarity $C_c = 50$ to design the pile according to the similarity of pile foundation, following Lin et al. [28]. When studying the seismic response of soil-pile systems, a gravity distortion model was adopted because of the difficulty of its additional counterweight [29]. Therefore, based on comprehensive consideration of various factors, the similarity ratio of other physical quantities was derived based on Buckingham's [30] π theorem. We ignored the similarity of gravitational acceleration and took length, elastic modulus, and mass density as the basic physical quantities [31]. Table 2 lists some of the parameters of this similarity law.

The selection of model materials for the shaking table test referred mainly to previous studies [8, 21]. According to the model's design parameters and the results of the ratio test on multiple groups of materials, sand was finally determined as the main material. Gypsum and talcum powders were selected as auxiliary materials while glycerin and water were selected as adhesive materials. The ratio of the model's composite materials is shown in Table 3; the physical and mechanical properties of these materials are shown in Table 4.

The pouring method for the pile body was cast-in-place, as shown in Figure 3.

To make the sliding process continuous, Teflon (polytetrafluoroethylene) was used to simulate the initial sliding surface of the slope. Teflon's effectiveness in simulating the sliding surface had been confirmed in previous studies [23, 32]. The material was pasted onto the surface of the bedrock along the contact boundary between the bedrock and the landslide materials. In the test, the anchor cable was simulated using a threaded rod with a diameter of 6 mm, of which the anchor length was 30 cm and the free length was 121 cm. To avoid the phenomenon of anchor cables crossing inside the slope body, we set a wide anchor-cable spacing and extended the anchor cable 20 cm above the pile head. This was convenient for prestressing the anchor cable and installing the springs.

In the process of preparation, sample materials were loaded into the model box by layering soil 10 cm thick, tamping each layer in the same way and thus ensuring the slope model's uniformity. As we prepared the model, we installed the antislide pile's stable structure and anchor-cable system in the target position, which is shown in Figures 4(a)–4(c). The accelerometer sensor was installed accordingly, as shown in Figures 4(d) and 4(e). Figure 5 shows the completed test model before the test.

The correct test results of dynamic soil-pressure gauges at each characteristic point before embedding indicate that there was no damage to dynamic soil-pressure gauges before model filling. During the test, the measurement signals of the dynamic soil-pressure gauges at S02, S06, S03′, and S05′ measurement points are distorted, and the measurement signals of the acceleration sensors at S06, S02′, and S05′ measurement points are distorted. It may be due to improper manual burying, which caused abnormal sensor test data. Therefore, it was not analyzed in the subsequent data processing.

2.4. Test Loading Scheme. After preparing the test model, we conducted the sine sweep by applying a series of sinusoidal waves with small amplitude but their frequencies being changed from 0.5 to 50 Hz gradually to check the frequency feature of the model system. The loading waveform, EL Centro wave, selected for this shaking table test was a seismic waveform widely used by experts and scholars in the field of seismic research. This waveform was described as featuring a first seismic wave with a maximum acceleration of more than 300 gal, according to a study conducted in the United States in 1940 [33]. The loading waveform was formed by an *XZ* bidirectional seismic wave synthesized from *X* and *Z* unidirectional seismic waves. The horizontal acceleration and vertical acceleration were applied synchronously. In addition, all data from the sensor were sampled during the test using a frequency of 187 Hz.

The seismic waves applied each time had the same shape, but their peak accelerations were different. We carried out load tests under three seismic conditions. The conditions for Case 1 presented low seismic acceleration, including vertical acceleration of 0.2 g and maximum horizontal acceleration of 0.4 g. Case 2 presented medium acceleration, including vertical acceleration of 0.4 g and maximum horizontal acceleration of 0.8 g. Case 3 presented high acceleration, including vertical acceleration of 0.7 g and maximum horizontal acceleration of 1.4 g. The loading sequence is shown in Figure 6.

Focusing on the soil-pile system's dynamic response and combining the research of previous studies in relevant

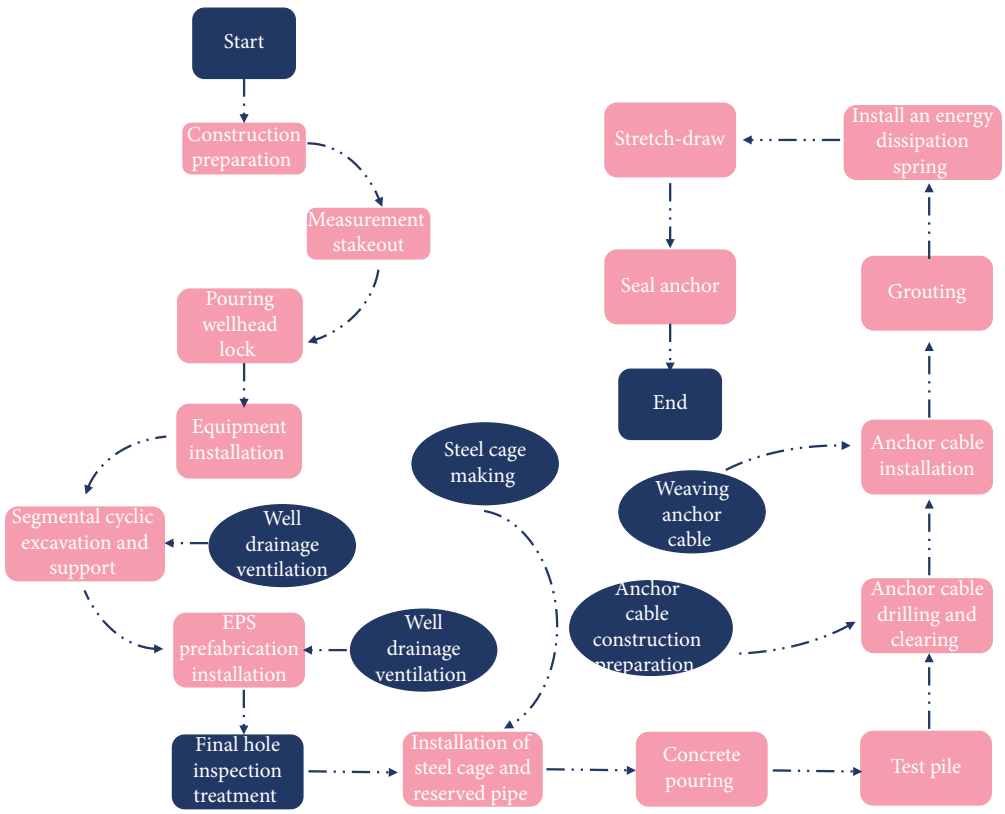

Figure 2: Process flowchart.

Table 2: Similarity ratio for shaking table test.

Physical quantity	Symbol and relational expression	Similarity ratio
Length (l)	$C_l = L_m/L_P$	1/50
Young's modulus (E)	$C_E = E_m/E_P$	1/50
Mass density (γ)	$C_\gamma = \gamma_m/\gamma_P$	1/1
Time (t)	$C_t = C_l 0.5$	1/7.07
Acceleration (a)	$C_a = C_E/C_l C_\gamma$	1/1
Cohesion (c)	$C_c = C_E$	1/50
Friction angle (φ)	1	1

aspects, we did not treat this test's seismic wave input using a similarity [34]. The original waveform input would have little impact for our research purpose. However, the original waveform is limited by the shaking table test itself. For example, it is difficult to simulate the time difference between successive arrivals of transverse and longitudinal waves in underground structures during earthquakes.

Owing to the Mesa sensor's abnormal acceleration, S01′ position at the bottom of the box in Case 1 was selected here to generate a time-history curve and Fourier spectrum, as shown in Figures 7(a) and 7(b).

3. Analysis of the Test Results

3.1. Deformation Characteristics of the Slope Model. Figure 8 summarizes the failure process of the slope under vibrations of different intensities. We inferred that the slope's internal instability was caused by slip along the sliding surface. This resulted in significant displacement. When we input a sinusoidal sweep frequency of 0.1 g on the Z direction, there was a small transverse crack to appear on the rear-edge surface of the unoptimized multianchor pile slope. When we input a sinusoidal sweep frequency of 0.1 g on the X direction, there was no obvious development of existing transverse cracks. Instead, the middle position of our optimized multianchor pile slope surface began to develop transverse cracks, and these tended to develop toward the unoptimized side.

Under the effect of low seismic acceleration, the model without optimization showed that its pile's lateral soil was destroyed. There was local breaking in the soil. Even the optimized model with a trailing edge showed an obvious transverse crack where we had not laid a border of Teflon material. This also gradually extended into the optimization and along the cross slope to the breaking in the soil. And the cracks are basically parallel and distributed in a "geese formation," as shown in Figure 8(a).

Under medium acceleration, the crack at the unoptimized leading edge continued to develop, and the crack at the front of the pile showed causation by extrusion of the pile. A deep lateral crack was also produced on the optimized side, from front to back, appearing later than the damage in the unoptimized pile, which is shown in Figure 8(a).

With high acceleration, large-scale collapse occurred on the front edge of the unoptimized side slope. Part of the front edge of the optimized side slope, near the unoptimized side, showed collapse. Other parts showed small penetrating

Table 3: Proportion of similar materials in the slope model.

Type	Mass mix ratio (%)					
	Sandy soil	Gypsum powder	Talcum powder	Glycerin	Bentonite	Water
Bedrock	80	2	5	10	—	3
Landslide materials	—	—	26.5	—	0.5	3
Pile	—	—	—	—	—	2

Table 4: Properties of the materials in the slope.

Type	Volume weight (g/cm^3)	Moisture content (%)	Compressive strength (MPa)	Cohesion (kPa)	Friction (°)
Bedrock	22.45	13.5	—	7.02	33.95
Landslide materials	16.5	14.2	—	15.2	29.75
Pile	20.4	—	4.5	—	—

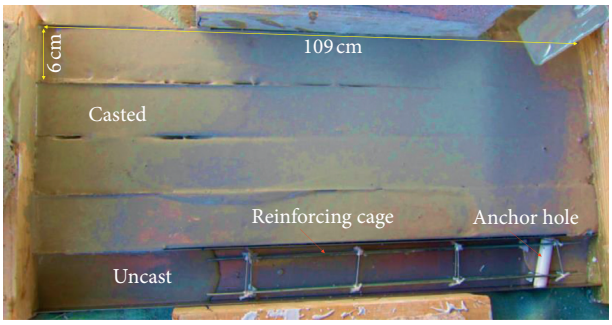

Figure 3: Casting site of model pile.

cracks. The whole posterior margin of the slope presented large-scale extrusion-deformation failure, existing cracks became wider, and there were phenomena revealing collapse and dislocation. As for the soil at the front of the pile, fractures caused by extrusion appeared on both sides. However, fractures on the unoptimized front were distributed in straight lines near the antislide pile. Meanwhile, fractures on the optimized front were distributed in the shape of a semicircle near Pile 1; those in Piles 2 and 3 were distributed in straight lines. At the middle part of the slope, several new cracks crisscrossed the unoptimized slope, as shown in Figure 8(a). Figures 8(b) and 8(c) show that on both sides of the model, the upper part of the slope's overlying material was separated from its initial position. Due to the strong force, it covered the pile top and finally deposited at the foot of the slope. The lower part slid downward. The maximum displacement of the unoptimized multianchor pile model was about 3.6 cm and its inclination was about 1.9°, while the anchor pile model's maximum displacement of the optimized multianchor pile model was about 1.1 cm and the inclination was about 0.6°.

Our analysis showed slope model deformation failure consistent with continuity of regional damage failure under the reciprocating action of XZ two-way seismic waves at different intensities. EPS foam was used as a shock-absorbing layer and an energy-dissipation spring was used for improving the self-coordinating devices of anchor head, improving the optimization of the slope. This optimization effectively contained continuous deformation and failure of the slope under strong earthquake conditions, showing an improved treatment effect.

3.2. Time-Domain Characteristics of Dynamic Response in Soil-Pile System. Taking seismic waves' loading at different intensities as the triggering factor (and based on the acceleration and dynamic soil-pressure test data), we selected three test positions to measure dynamic response. These were S01, S01′ (in the bedrock), S03, S03′ (near the sliding surface), and S06, S06′ (on the upper part of the landslide material). All three were located on the mountain side of the pile body. Acceleration and dynamic soil-pressure response were recorded at the three test positions.

3.2.1. Dynamic Response Characteristics of Acceleration Time-History. To clearly understand the time-history variations in acceleration for our multianchor pile under different earthquake intensities, we analyzed the time-history curve and peak acceleration of the model over time.

It can be seen from Figures 9(a) and 9(b) that under low seismic acceleration, the peak values of XZ direction acceleration response at S01, S03, and S06 on the optimization side were 4.11 m/s^2, 4.40 m/s^2, and 4.62 m/s^2, respectively. The peak values of XZ direction acceleration response at S01′, S03′, and S06′ of the unoptimized side were 4.35 m/s^2, 4.35 m/s^2, and 5.01 m/s^2, respectively. According to Figures 9(c) and 9(d), the peak values of XZ direction acceleration response at S01, S03, and S06 on the optimized side were 16.58 m/s^2, 16.42 m/s^2, and 20.44 m/s^2, respectively, under high accelerations. The peak values of XZ direction acceleration response at S01′, S03′, and S06′ of the unoptimized side were 15.83 m/s^2, 17.00 m/s^2, and 23.81 m/s^2, respectively. Under the highest seismic acceleration, all acceleration responses increased.

As can be seen from Figure 10, under low and medium seismic accelerations, optimized and unoptimized lateral acceleration response increase with the increase of elevation. Under high acceleration, the response of the upper part of S06 (S06′) was the largest regardless of optimization, followed by the acceleration responses of the bedrock S01 (S01′) and of the position near the sliding surface S03 (S03′). This indicates the EPS on the side of the pile body played a role in energy mitigation and dissipation, which has a significant effect on slope body and slide surface but no obvious effect on bedrock S01 (S01′).

3.2.2. Dynamic Response Characteristics of Dynamic Soil-Pressure Time-History. To clearly understand dynamic

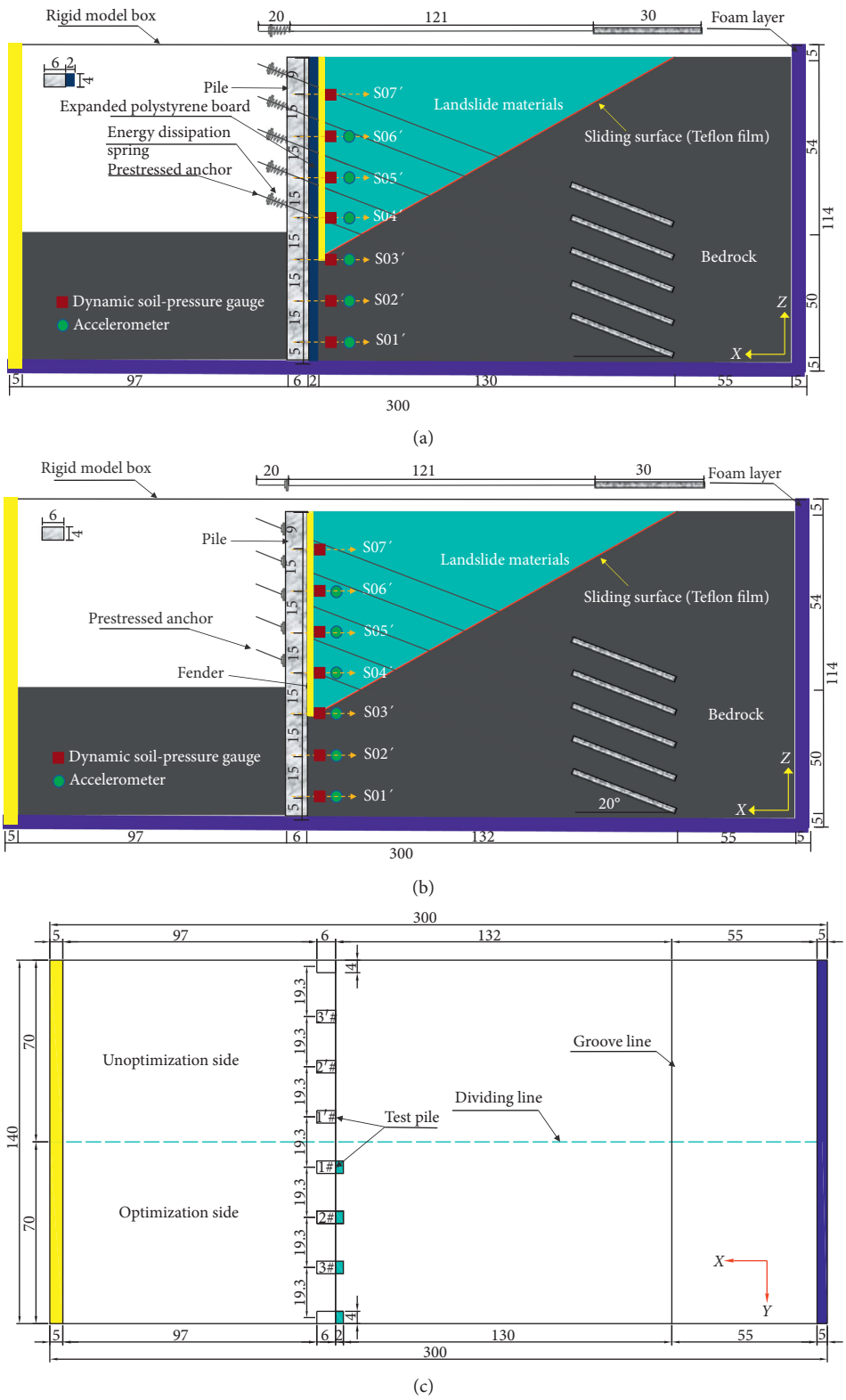

Figure 4: Shaking table test model design drawing (unit: cm). (a, b) The profile diagram of the optimized multianchor cable antislide pile and the unoptimized multianchor cable antislide pile. (c) The top view of the vibration platform side slope model. For the optimized multianchor pile, the pile is prefabricated in advance, and a layer of EPS foam is pasted on the side of the pile mound. The height × width × thickness of the EPS foam is 109 cm × 4 cm × 2 cm, as shown in the dark blue part of Figure 4(a). In addition, an energy-dissipating spring self-coordinating device is set between the anchor head and pile. Screws and gaskets are used to simulate anchors to lock the anchor, and the prestress is applied by adjusting the screws. It uses screws and washers to simulate anchors for anchoring and adjusts screws to apply prestress.

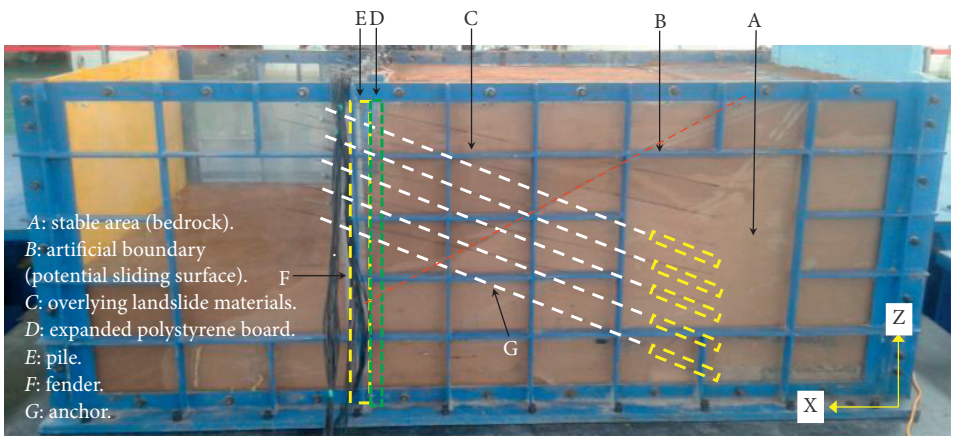

(a)

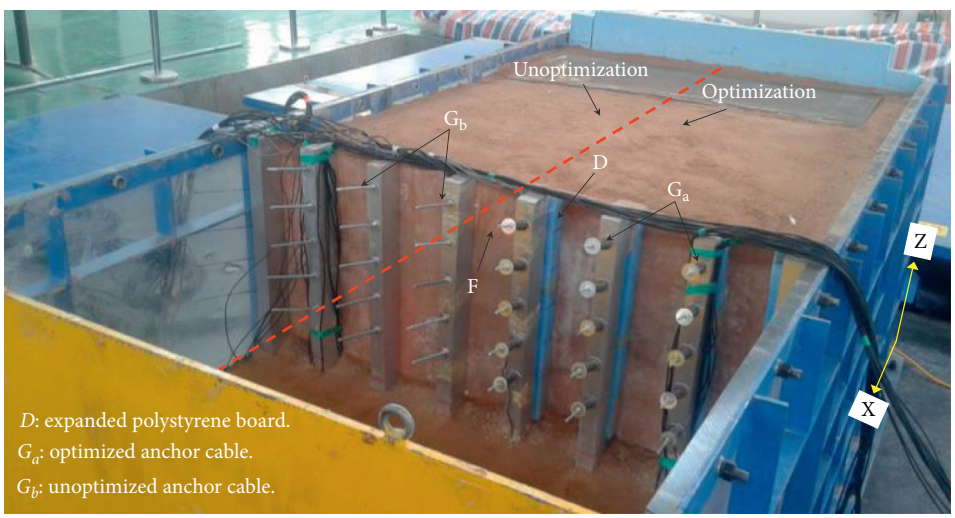

(b)

Figure 5: Physical image of shaking table test model. (a) Front view of the test model completed before the test. (b) 45° side view of the test model completed before the test. X and Z indicate the direction along the long side of the model box and perpendicular to the table top, respectively.

soil-pressure change along the elevation of multianchor piles under different earthquake intensities, we analyzed the time-history curve of dynamic soil-pressure and peak values for dynamic soil-pressure in the model over time.

According to the analysis of dynamic soil-pressure represented in Figures 11(a) and 11(b), we showed the peak values of XZ response to dynamic soil-pressure for S01, S03, and S06 (on the optimized side) under low seismic acceleration. The values were 0.22 kPa, 0.11 kPa, and 1.70 kPa, respectively. The peak values at S01′, S03′, and S06′ (on the unoptimized side) were 0.27 kPa, 0.39 kPa, and 6.53 kPa, respectively. As shown in Figures 11(c) and 11(d), under high acceleration, the peak values of the XZ response to dynamic soil-pressure at S01, S03, and S06 (optimized side) were 36.77 kPa, 47.89 kPa, and 40.43 kPa, respectively. The peak values at S01′, S03′, and S06′ (unoptimized side) were 36.02 kPa, 46.52 kPa, and 49.79 kPa, respectively. At the highest seismic acceleration, all dynamic soil-pressure responses became greater.

As shown in Figure 12, our analysis revealed that with low seismic acceleration, the dynamic soil-pressure response at the optimal position near the lateral sliding moving surface S03 was the smallest; the upper part of the overlying sliding body S06 was the largest. The optimized position of the bedrock S01 is slightly less than the unoptimized value. Under high acceleration, the highest dynamic soil-pressure response appeared at positions near the sliding surface S03, followed by that at the upper part of the overlying sliding body S06. The lowest appeared at the position of the bedrock S01.

According to the deformation characteristics of EPS in our test, the elastic modulus of EPS foam is only 2.4 MPa, and the compression process is basically similar either in a three-direction stress state or in a unidirectional stress state. When the axial strain $\varepsilon_a = 5\%$, the stress-strain curve shows a significant turning point and EPS foam begins to show elastic-plastic behavior. When the confining pressure is very small, there is limited influence on the stress-strain relationship and yield strength [35]. This indicates that EPS foam has no obvious effect on dynamic soil-pressure buffering for bedrock S01 under low seismic acceleration. Under high acceleration, the dynamic soil-

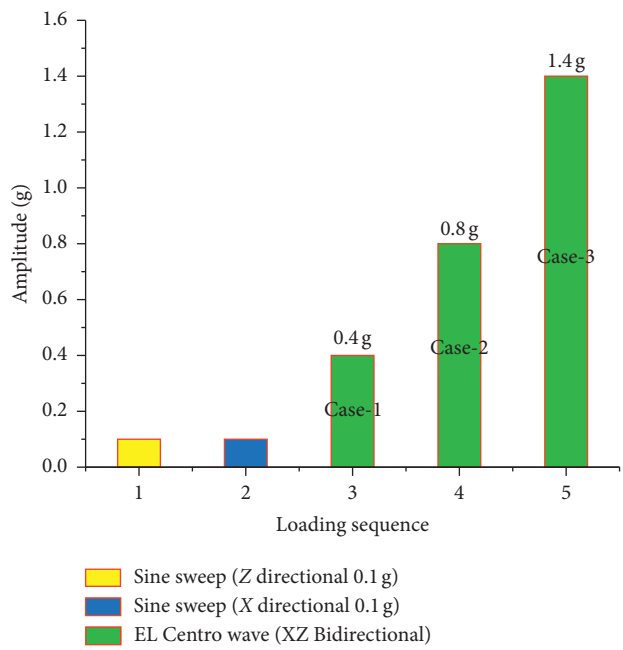

Figure 6: Loading sequence of shaking table test.

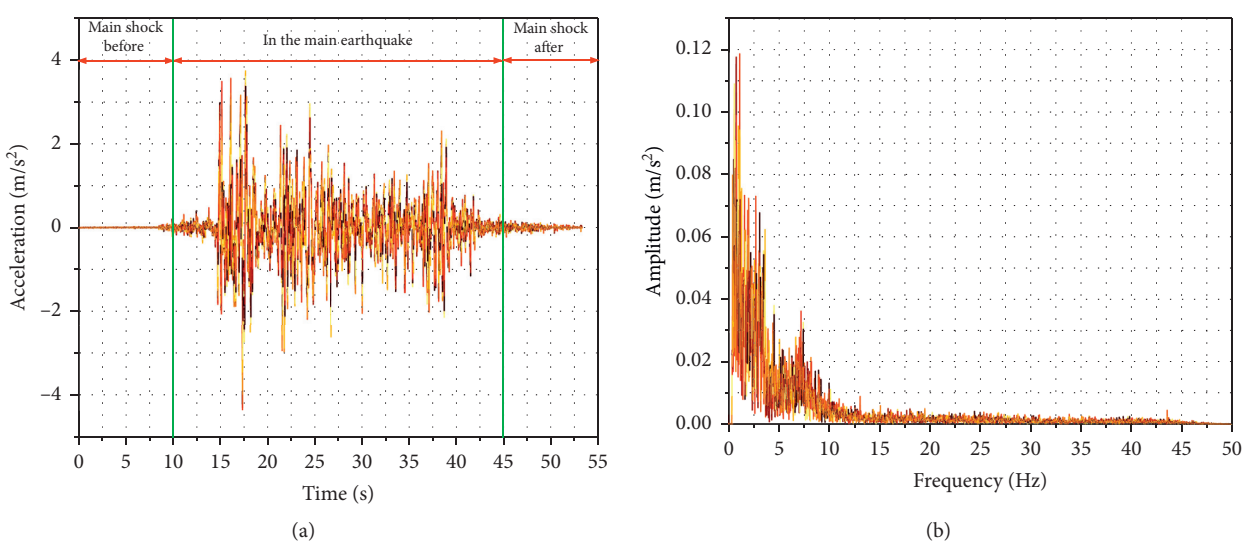

Figure 7: (a) Acceleration time-history curve. (b) Fourier spectrum.

pressure at the position of the overlying slide body S06 shows significant improvement. The main reason for this is the energy-dissipation spring's stretching and deformation; it has a significant effect on the energy dissipation in the slope body and slide surface, which plays a role in the mitigation of energy dissipation. EPS foam has a significant effect on the energy dissipation of bedrock.

3.3. Spectral Characteristics of Dynamic Response in Soil-Pile System. Figures 9 and 11 show the dynamic time-history law of acceleration and dynamic soil-pressure for the multi-anchor pile model. The spectral response characteristics and the relationship between the lateral acceleration of the multianchor pile and the dynamic soil pressure is further clarified. This was obtained using a fast Fourier transform (FFT) under the condition of a low and high seismic Fourier spectrum, comparative analysis of characteristic spots on acceleration, and characteristics of the dynamic soil-pressure difference spectrum.

According to the data analysis presented in Figure 13, the acceleration spectrum curves for each characteristic point change uniformly under different seismic actions. Under low seismic acceleration, the predominant frequency is mainly concentrated in the range of 0.5–4 Hz, and the maximum amplitude frequency is 1.15 Hz. The acceleration spectrum response at the position of S01′ in our test expressed the maximum. The dynamic soil-pressure spectrum curve changed

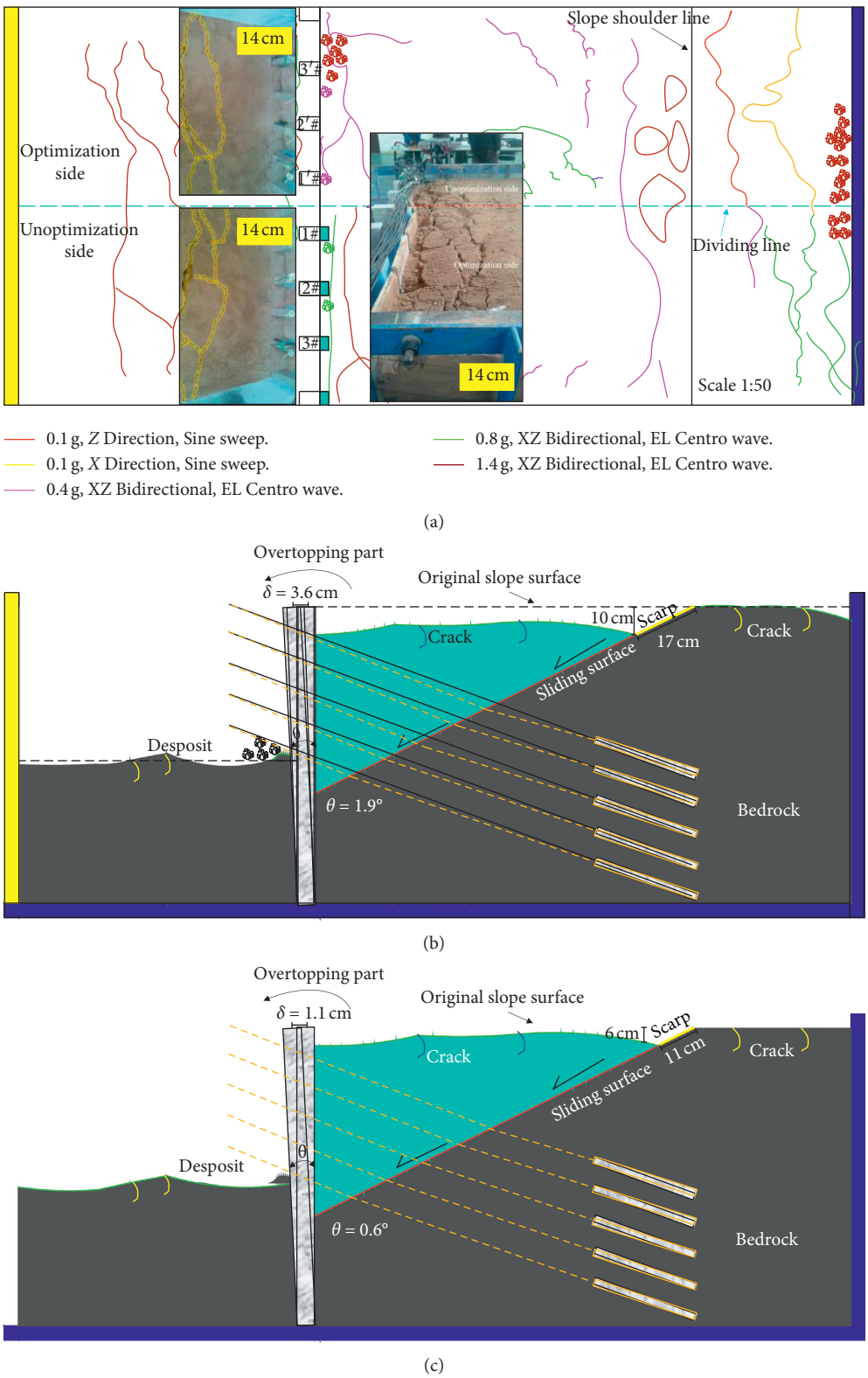

Figure 8: Shaking table model test feature image. (a) Posttest behavior of multianchor pile model under low, medium, and high acceleration. (b) Phenomena of section test after high acceleration on the unoptimized side of multianchor pile model. (c) Phenomena of section test after high acceleration on the optimized side of multianchor pile model. The green dotted line indicates the overtop portion and its deposition area due to high acceleration. The maximum displacement (δ) and inclination (θ) of the pile block were also indicated.

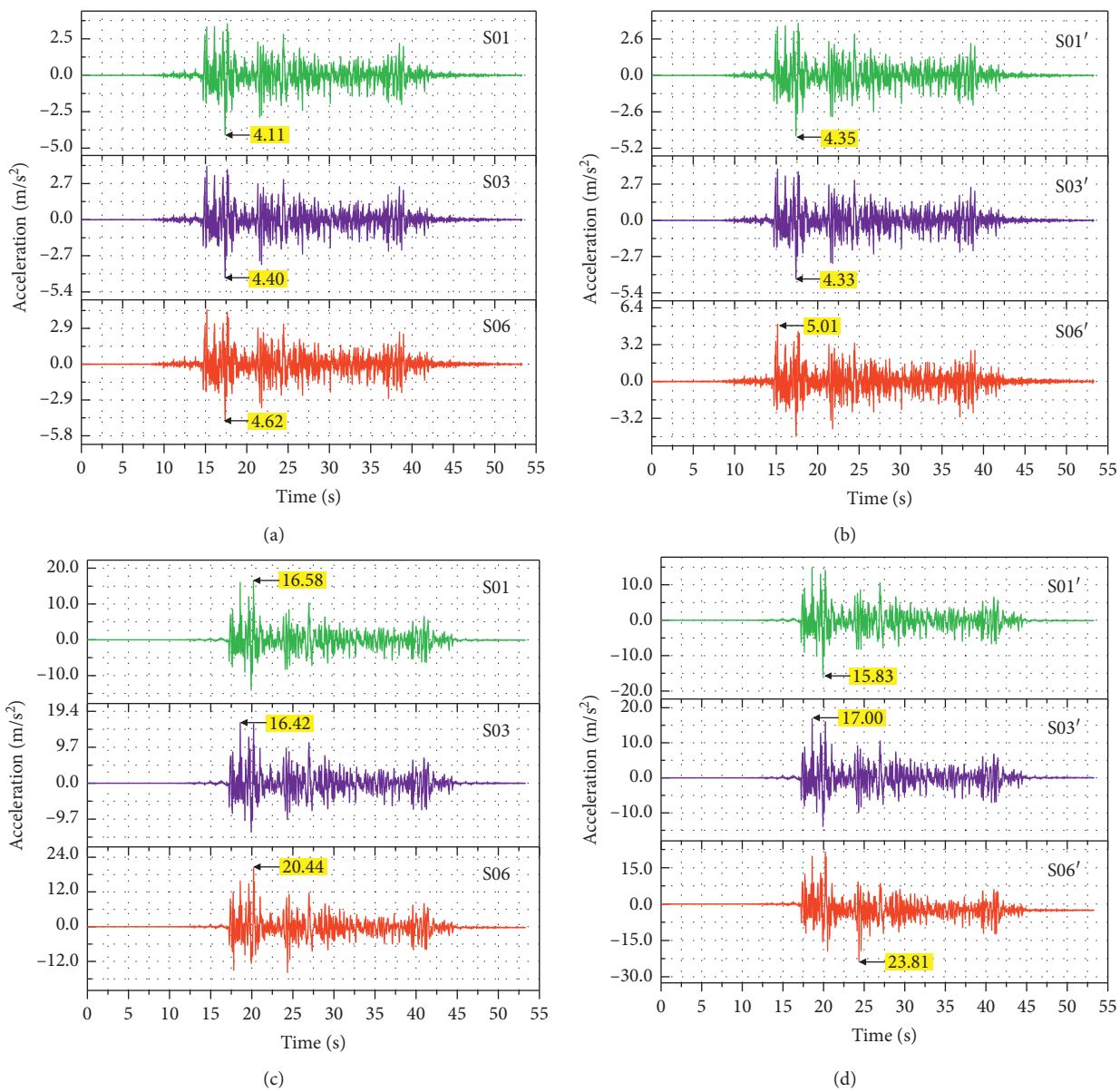

Figure 9: Acceleration time-history curve. (a) Case 1 working condition: optimized pile acceleration time-history curve. (b) Case 1 working condition: unoptimized pile acceleration time-history curve. (c) Case 3 working condition: optimized pile acceleration time-history curve. (d) Case 3 working condition: unoptimized pile acceleration time-history curve.

significantly: the optimized side showed S06 > S03 > S01 while the unoptimized side showed S06′ > S03′ > S01′. Predominant frequencies were mainly concentrated in range of 1–3 Hz. With high acceleration, with predominant frequencies of 0.5–4 Hz, the optimized side showed S01 > S06 > S03 and the unoptimized side showed S01′ > S06′ > S03′. When the predominant frequency was in the range of 4–10 Hz, the optimized side showed S01 > S03 > S06 and the unoptimized side showed S03′ > S01′ > S06′. The predominant frequency of dynamic soil-pressure was mainly concentrated in the range of 0.5–5 Hz. The spectral distribution curves of S03 and S03′ at the sliding surface position are basically the same, and the spectral values of S03′ are all greater than those for S03, which shows the same behavior at the bedrock level.

The spatial distribution of amplitude for the acceleration spectrum is characterized by outstanding response to the unoptimized amplitude in the pile structure. The spatial distribution of the dynamic soil-pressure spectrum shows that a multianchor pile is affected by the strength and buried depth of the embedded stratum, which can easily become the weak link in subsequent seismic resistance. The shock-absorbing layer of EPS foam and the self-coordinating device of energy-dissipation springs (improving anchor heads) have

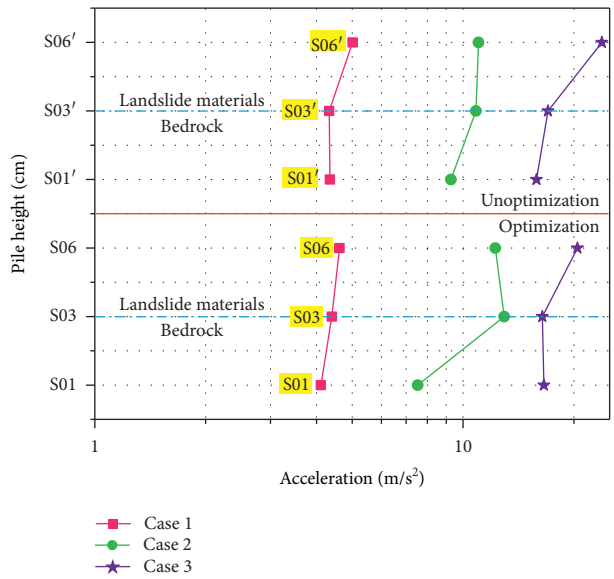

Figure 10: Acceleration peak change curve. In order to facilitate data processing and highlight the essential meaning of physical quantities, normalization has been performed after selecting the dimensional unit system. Figures 12, 13, and 15 in the text were all processed by this method.

cushioning effects on pile's seismic dynamic response, but their effects are different. The dynamic response of acceleration only serves to dissipate energy without changing spectrum characteristics. The response in dynamic soil-pressure not only dissipates energy but also shows damping characteristics, due to its expansion and deformation changes and the spectrum characteristics of dynamic soil-pressure of the structure.

4. Discussion

4.1. Correlation Characteristics of Frequency Spectrum Amplitude Variation. Figure 13 shows spectral variations in low and high seismic accelerations and dynamic soil-pressure. We calculated the amplitude peak of characteristic points under various earthquake conditions by using a statistical probability scatter matrix to further quantify the characteristics of the amplitude difference between the acceleration and the dynamic soil-pressure spectrum curve. This allowed us to more intuitively demonstrate the correlation between seismic acceleration and dynamic soil-pressure response.

The correlation analysis of the acceleration amplitude scatter matrix presented in Figure 1(a) shows that the response variables of seismic acceleration are all positively correlated. The correlation coefficient between 0.4 g and 0.8 g of ground-motion response is 0.88193, marking a strong correlation for the response of ground-motion acceleration. The scatter diagram shows that the 95% binary normal density ellipse is relatively flat, extending along the diagonal. This indicates that side piles show a strong linear correlation between their response under low and medium accelerations. The correlation coefficient between 0.4 g and 1.4 g of ground-motion response is 0.18295; the greater the difference in the ground-motion response, the weaker the correlation coefficient. The correlation coefficient between 0.8 g and 1.4 g is 0.49941, and the correlation between responses in ground-motion acceleration is weak. The scatter diagram shows that the 95% binary normal density ellipse is circular and does not extend along the diagonal direction. This indicates no correlation between acceleration response magnitudes in mountain side piles before the repeated occurrence of an earthquake in the same area.

The results show that the amplitude and spectrum characteristics of the foreshock sequence, before an earthquake reaches 1.4 g, are quite different. Especially for mountain side piles, the ground-motion characteristics of foreshocks are not simply repeated superpositions of the ground-motion sequences across all levels. When the foreshock action sequence (before the earthquake) reaches 1.4 g and is not taken into account, the nonlinear acceleration-response demand of the ground motion on the structure will be underestimated.

According to correlation analysis of the scatter matrix graph on dynamic soil-pressure amplitude in Figure 14(b), the seismic response variables of dynamic soil-pressure are all positively correlated, but the overall correlation coefficients are relatively small. The correlation coefficient between 0.4 g and 0.8 g and between 0.4 g and 1.4 g of ground-motion response is 0.4848 and 0.78387, respectively, and that between 0.8 g and 1.4 g is 0.79831. There is strong correlation between dynamic soil-pressure responses to earthquakes in each group, and the greater the difference in ground-motion response, the stronger the correlation coefficient. This indicates that there is no correlation between a pile's dynamic soil-pressure response to foreshock magnitude before the repeated occurrence of an earthquake in the same area.

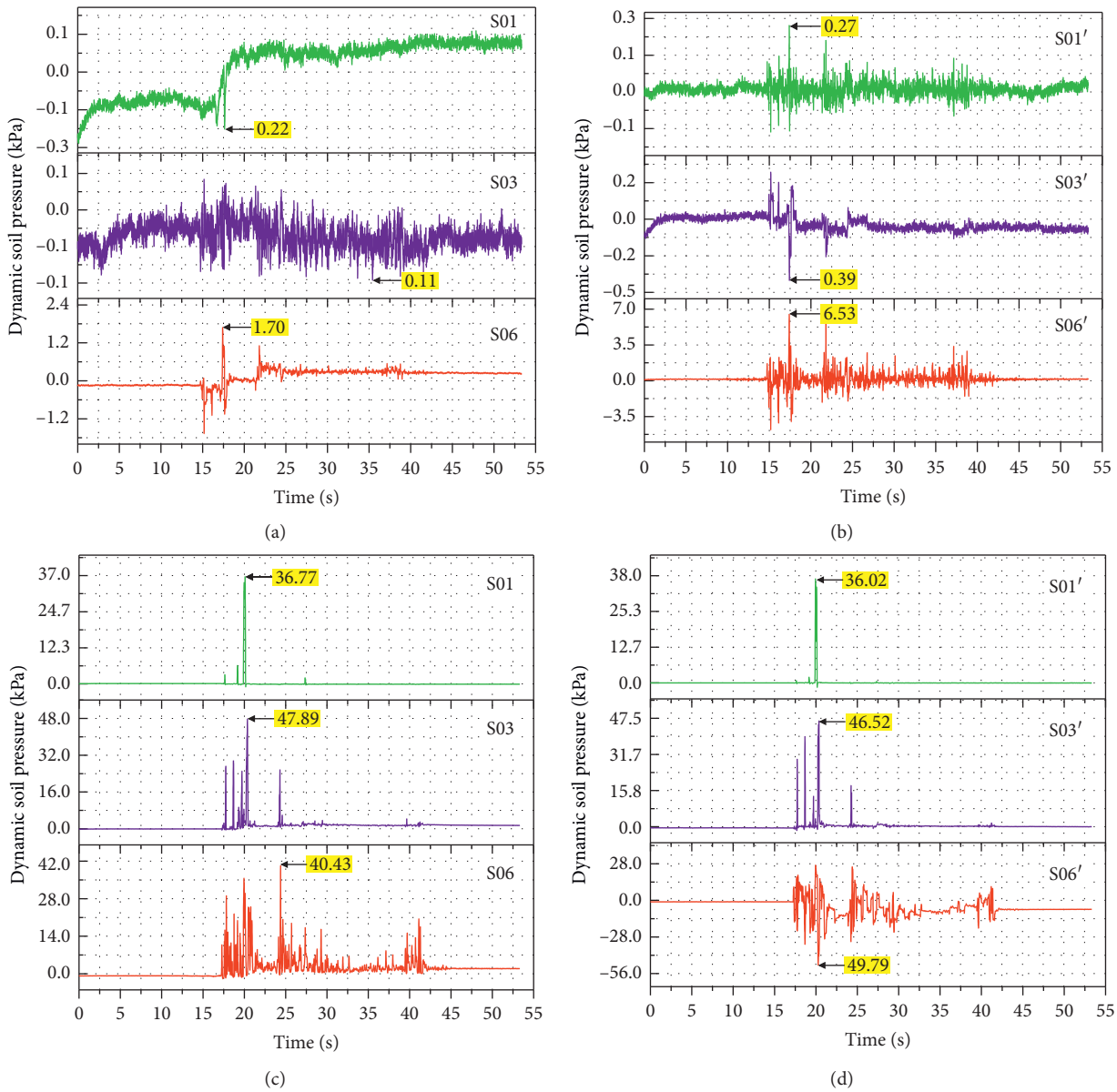

Figure 11: Dynamic soil-pressure time-history curve. (a) Case 1 working condition: optimized pile dynamic soil-pressure time-history curve. (b) Case 1 working condition: unoptimized pile dynamic soil-pressure time-history curve. (c) Case 3 working condition: optimized pile dynamic soil-pressure time-history curve. (d) Case 3 working condition: unoptimized pile dynamic soil-pressure time-history curve.

The results show that the amplitude and spectrum characteristics of dynamic soil-pressure differ significantly before an earthquake reaches 1.4 g. The dynamic soil-pressure of a pile on a mountain side has a strong correlation, and, as shown in Figure 6, the pile-soil system has continuity effects in regional damage and destruction. Therefore, the effect of such continuity should be considered effectively for improved seismic design in the future.

4.2. Spectrum Difference Characteristics at Different Vibration Stages. To further clarify the variation of frequencies in a specific week [23], different vibration periods of seismic waves were loaded according to Figure 5(a). These are divided into the following three vibration stages. At 0–10 s, they correspond to the main shock-wave front. At 10–45 s, they correspond to the main shock wave (whose Fourier spectrum is hereinafter referred to as the dominant amplitude). At 45–55 s, they correspond to the main shock wave after. The characteristic points of S01 and S06 on the optimized side of our model were selected here, and the spectrum curves of acceleration and dynamic soil-pressure are shown in Figure 15.

Under low seismic acceleration, the variation of acceleration spectrum curves before, during, and after the main shock wave are basically the same, characterized by significant response at the S06 position. However, the dominant frequencies of various vibration periods differ

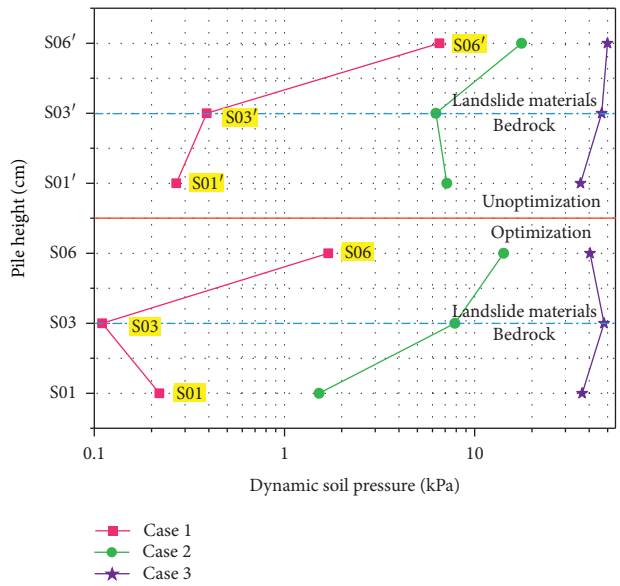

Figure 12: Dynamic soil-pressure peak change curve.

significantly. Before the main shock wave, as shown in Figure 15(a), a dominant frequency in amplitude of acceleration at S01 and S06 is 3.68 Hz and that in dynamic soil-pressure at the same points is 0.73 Hz. During the main shock wave, as shown in Figure 15(b), the dominant frequency in amplitude of acceleration for S01 and S06 is 1.51 Hz and that in amplitude of dynamic soil-pressure is 1.17 Hz. After the main shock wave, the dominant frequencies of acceleration amplitude at these two points reach 6.83 Hz, and the dominant frequencies of dynamic soil-pressure amplitude are 0.68 Hz and 0.55 Hz. The phase of the acceleration spectrum for S06 lags behind that for S01, indicating that the difference in acceleration hysteresis along the elevation is mainly caused by the propagation stage after the main shock wave, as shown in Figure 15(c).

With high acceleration, spectrum curves for 10–45 s and 45–55 s are very different. Before the main shock wave, the dominant frequency of the acceleration amplitude at S01 and S06 is 3.68 Hz, and the dynamic soil-pressure response at both points is significantly greater than the acceleration. The dominant frequencies are 0.5 Hz and 0.6 Hz, respectively. In the interval of 0.5–2 Hz, the dynamic soil-pressure spectrum response at S01 is greater than that at S06. In the interval of 2–10 Hz, the dynamic soil-pressure spectrum response at S06 is greater than that at S01, as shown in Figure 16(a). After the main shock wave, there are two dominant frequencies of acceleration at S01 and S06: 0.75 Hz and 6.96 Hz, respectively. The dominant frequencies of dynamic soil-pressure amplitude at S01 and S06 are 0.82 Hz and 1.50 Hz, respectively. When the dominant amplitude is 10–45 s, the dominant frequency in amplitude of acceleration at both points is 1.51 Hz and, as shown in Figure 16(b), and that in amplitude of dynamic soil-pressure is 0.83 Hz and 1.17 Hz, respectively. With high acceleration, the two time periods after dominant amplitude (10–45 s and 45–55 s) indicate that the main frequency of seismic wave response at S06 begins to fail when the slope body model behind the pile is deformed, and the dynamic soil pressure will change. The phenomenon shown in our test appears in Figure 8(b).

4.3. Characteristics of Ground-Motion Input Energy of Slope Model. Liu and Shen [37] found through theoretical analysis that damping ratio has little effect on total seismic input energy. The total input energy of seismic waves is equivalent to the velocity spectrum (damping ratio 5%) and the pseudo-velocity spectrum (damping ratio 5%). The two have good consistency. Based on the relative input low-frequency energy control theory described by previous studies [38, 39], the total input energy for our structure was simplified. That is, the influence of the structure's mass on total input energy was eliminated, and the structure's energy-equivalent velocity spectrum was analyzed. Based on the above range of effective frequency accelerometers and the input power spectral amplitudes, we used the SPECTR program to calculate spectral responses of acceleration at various points. In this way, we obtained the pseudo-velocity spectrum of seismic waves, as shown in Figure 17.

Figure 17 shows the seismic input energy spectrum under the normalized intensities of low and high seismic accelerations. On the whole, the energy spectrum for the total ground-motion input on the optimized side was less than that on the unoptimized side. Compared with the unoptimized side, the optimized side is reduced by 19.45% under low seismic acceleration. Under high acceleration,

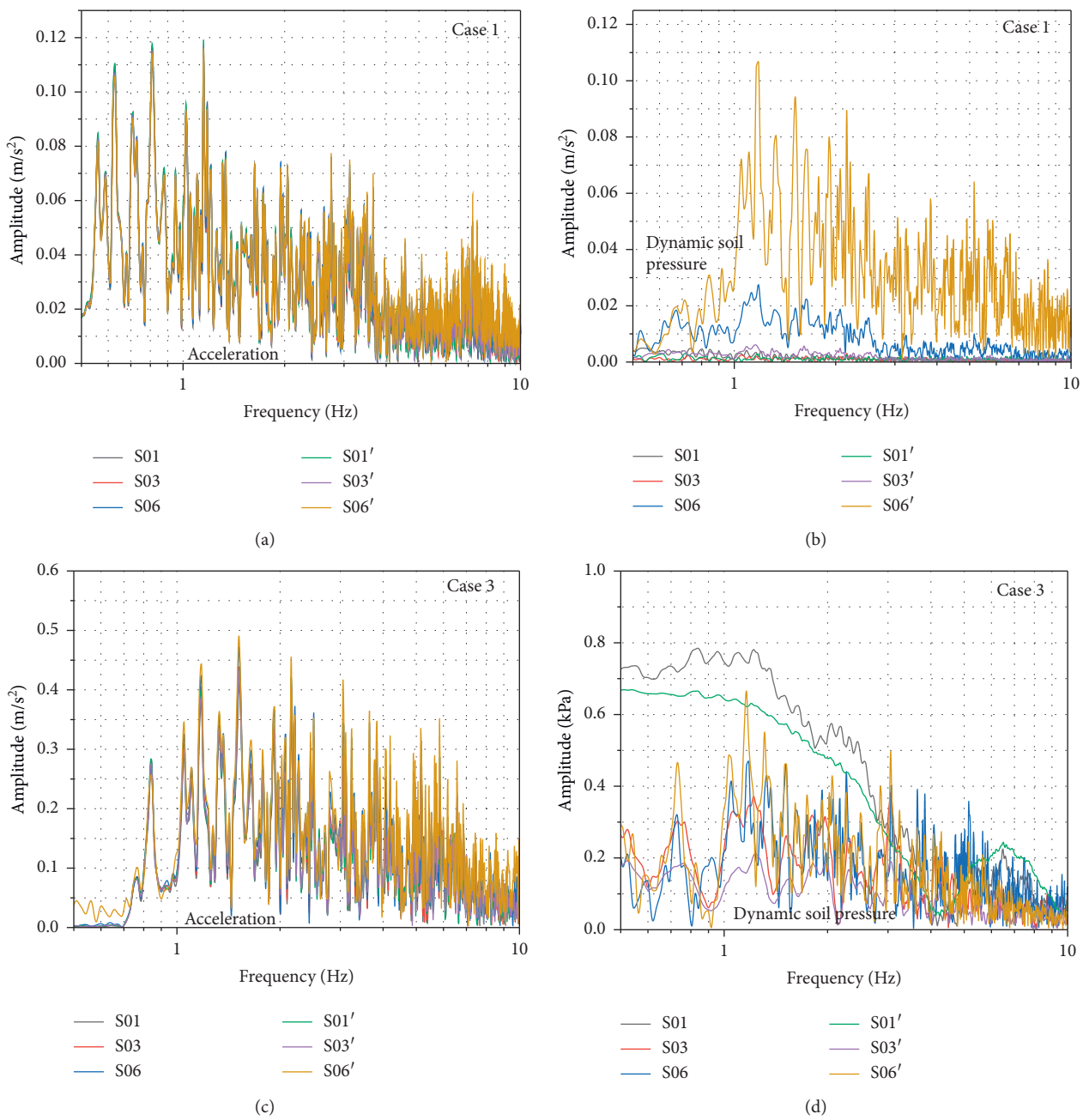

Figure 13: Spectrum curve. (a) Spectrum curve of low seismic acceleration. (b) Spectrum curve of low seismic dynamic soil-pressure. (c) Spectrum curve of high acceleration. (d) Spectrum curve of high seismic dynamic soil-pressure.

the optimized side compared to the unoptimized side decreased by 23.69%. Under low seismic acceleration, the energy-spectrum distribution for unoptimized lateral acceleration and dynamic soil-pressure seismic input were relatively stable. The acceleration manifested mainly in three stages: ascending, stationary, and descending stages. The frequency during the stationary stage was mainly concentrated in the low-frequency range of 2–6 Hz, a preliminary indication that the energy distribution was related to the spectrum. In this low-frequency range, the total input energy for dynamic soil-pressure was greater than the acceleration, and the relative error of the total input energy was 22.98%. After exceeding 10 Hz, the total input energy value of the dynamic soil-pressure was greater than the acceleration.

After optimization, there was a big difference in the energy-spectrum distribution of acceleration and dynamic soil-pressure. The total input energy value of acceleration was greater than that of dynamic soil-pressure. The latter was affected by the two-way loading seismic wave spectrum, resulting in two obvious peaks on the total input energy spectrum for dynamic soil-pressure, both greater than 10 Hz. After that, the total input energy value of dynamic soil-pressure was greater than the acceleration.

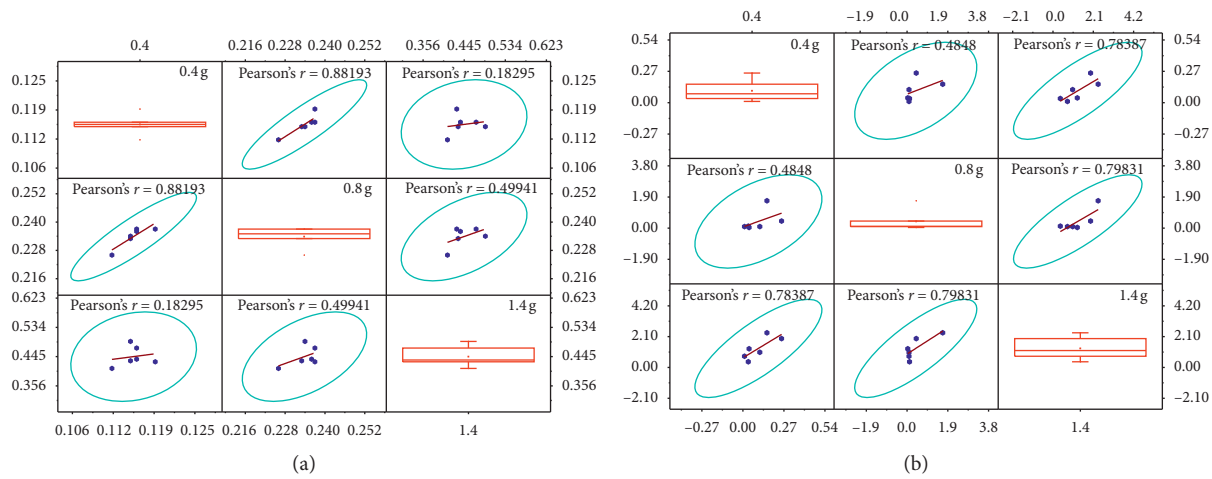

Figure 14: Amplitude scatter matrix plot with dimension 3. (a) Scatter plot of acceleration amplitude matrix with dimension 3. (b) Scatter plot of dynamic soil-pressure amplitude matrix with dimension 3. The multivariate blue dots in the figure above represent the scattered distribution of amplitude values. Cyan ellipse represents 95% bivariate normal density ellipse displayed in each scatter diagram, and the narrowness of the ellipse reflects the correlation degree of variables. If the ellipse is circular and does not extend diagonally, there is no correlation between the variables. If the ellipse is narrow and extends along the diagonal direction, there is a correlation between variables [36].

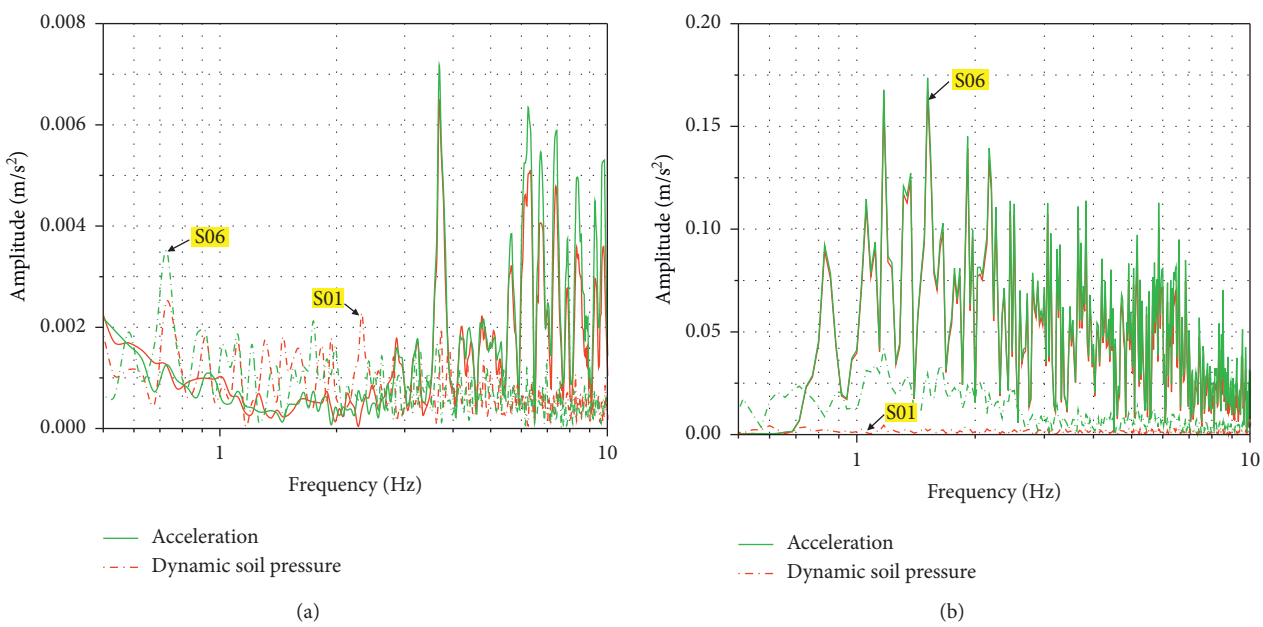

Figure 15: Continued.

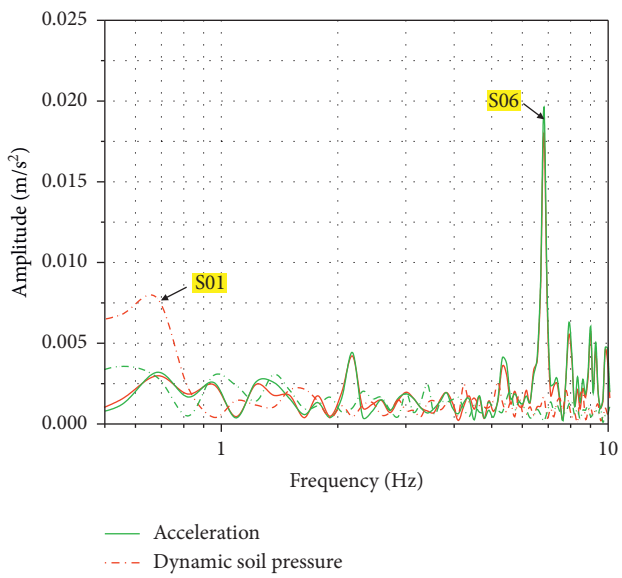

(c)

Figure 15: Acceleration and dynamic soil-pressure Fourier spectrum curves at different stages of low seismic acceleration. (a) Fourier spectrum curves in main shock-wave front acceleration and dynamic soil-pressure of low seismic acceleration. (b) Fourier spectrum curves in main shock-wave acceleration and dynamic soil-pressure of low seismic acceleration. (c) Fourier spectrum curves in main shock wave after acceleration and dynamic soil-pressure of low seismic acceleration.

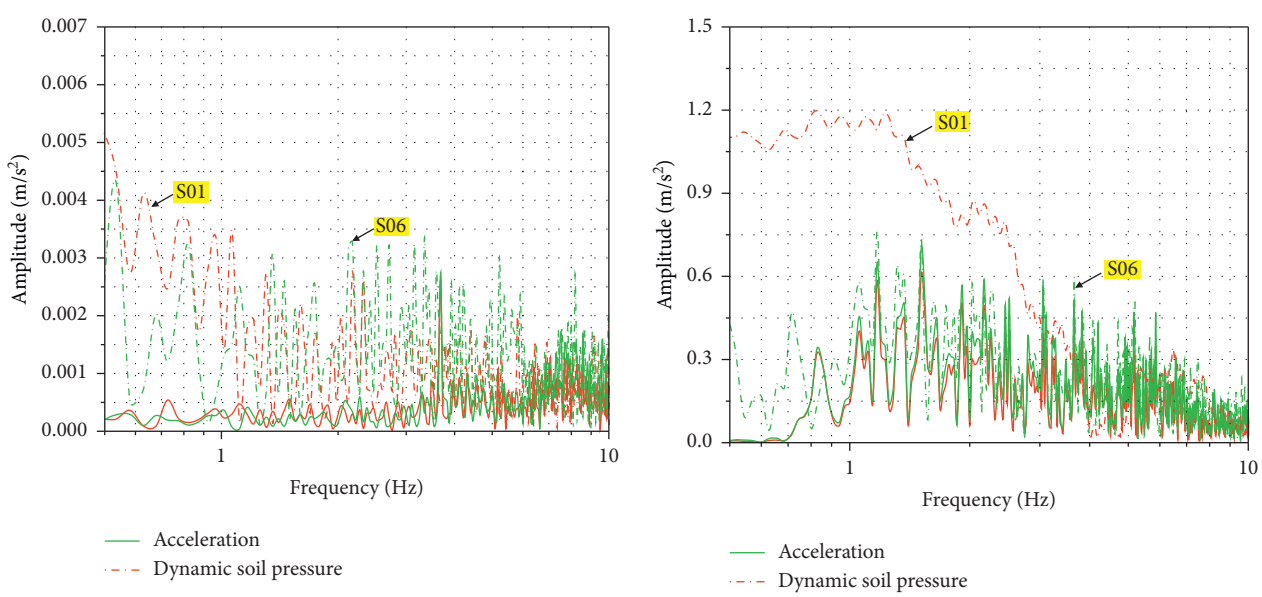

(a) (b)

Figure 16: Continued.

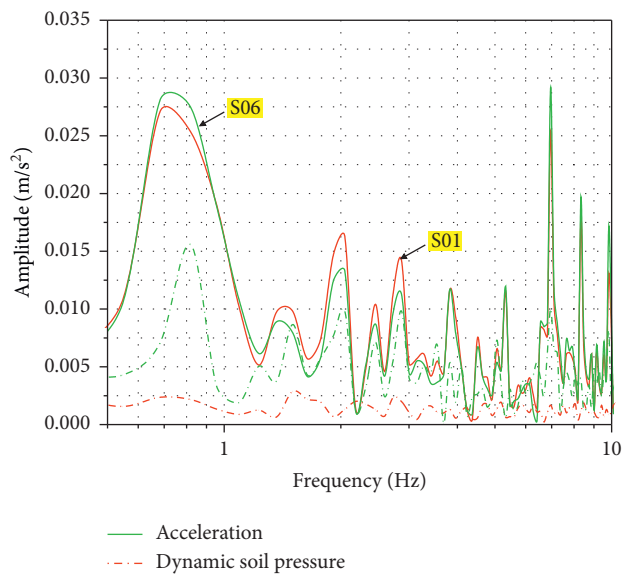

(c)

Figure 16: Acceleration and dynamic soil-pressure Fourier spectrum curves at different stages of high acceleration. (a) Fourier spectrum curves of the main shock-wave front acceleration and dynamic soil-pressure of high acceleration. (b) Fourier spectrum curves of phase acceleration and dynamic soil-pressure in the main shock wave of high acceleration. (c) Fourier spectrum curves of phase acceleration and dynamic soil-pressure after the main shock wave of high acceleration.

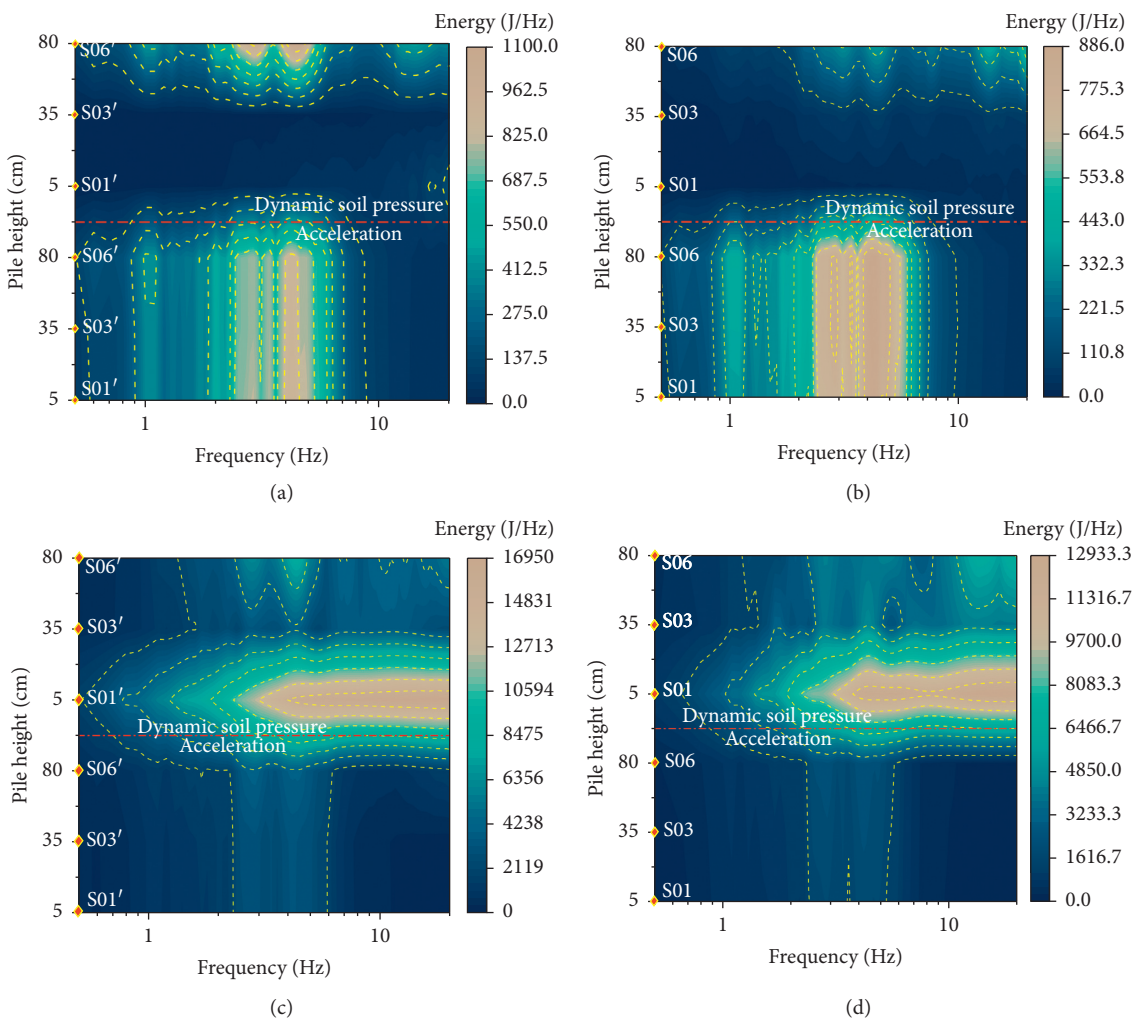

Figure 17: Energy spectrum. (a) Unoptimized side energy spectrum for low seismic acceleration. (b) Optimized side energy spectrum for low seismic acceleration. (c) Unoptimized side energy spectrum for high acceleration. (d) Optimized side energy spectrum for high acceleration.

Under high acceleration, total input energy of dynamic soil-pressure is greater than acceleration. According to our calculation results, pile acceleration is distributed in an orderly manner. Under the influence of the frequency spectrum of our bidirectional loading seismic wave, the total input energy spectrum of acceleration showed two obvious peaks, and the dynamic soil-pressure distribution of the pile body was disordered. Under the influence of surrounding media, the difference of total energy input in the low-frequency range is more significant, affected by the position of characteristic points of the pile body. With the increase of structure height, the total input energy spectrum tends to decrease.

5. Conclusions

We aimed to study dynamic soil-pressure and acceleration dynamic response's spatial variations, in soil slopes strengthened using multianchor piles under earthquake conditions. The optimal seismic performance of the multianchored pile was discussed. Based on the special form of multianchor piles' reinforcement, we put forward the optimal design scheme of using EPS sheets as damping layers and energy-dissipation springs for improving the self-coordinating devices of anchor head. In this study, we conducted a series of multianchor pile shaking table tests. The results are summarized as follows:

(1) Under the reciprocating action of seismic waves of different intensity, nonlinear reciprocating displacement occurs to the slope body. The slope model shows the continuous effect of spatially coupled deformation caused by regional damage and failure.

(2) The low-frequency (≤10 Hz) seismic waves have a great influence on the structure. For the dynamic response of acceleration, the optimized structure only plays a role of energy dissipation without changing the spectrum characteristics. The response in dynamic soil-pressure not only dissipates energy but also shows damping characteristics, due to its expansion and deformation changes and the spectrum characteristics of dynamic soil-pressure of the structure.

(3) The difference of acceleration hysteresis along the elevation is mainly caused by the propagation stage after the main earthquake. The correlation between dynamic soil-pressure and acceleration response of each group before the pile occurred in the same seismic area is very weak. The ground-motion characteristics of foreshocks are not simply repeated superposition of all levels of ground-motion sequences, but the soil-pile system has the continuous effect of regional damage and destruction.

(4) Under the influence of the spectrum of the loaded seismic wave, there are two obvious peaks in the total input energy spectrum of acceleration and dynamic soil-pressure. The energy-spectrum distribution of acceleration seismic input is orderly and stable, and the dynamic soil-pressure distribution of pile is disordered.

(5) Under high acceleration, EPS foam will have plastic deformation and increase the relative displacement value on the optimized side, which will easily cause the bulging failure or shear failure of multianchor point pile at the position of sliding surface. Under the influence of the strength and buried depth of the embedded stratum, multianchor piles easily become the weak link in terms of subsequent seismic resistance.

Data Availability

The data used to support the findings of this study are available from the corresponding author upon request.

Conflicts of Interest

The authors have no conflicts of interest to declare.

Authors' Contributions

Honggang Wu performed the technological development. Lifang Pai prepared and edited the manuscript. Hao Lei proofread the manuscript. Honggang Wu and Lifang Pai and contributed equally to this work and should be considered co-first authors.

Acknowledgments

The authors gratefully acknowledge the financial support provided by the National Key R&D Program of China (no. 2018YFC1504901) and Natural Science Foundation of Gansu Province (no. 145RJZA068). The authors would also like to thank TopEdit (http://www.topeditsci.com) for English language editing of this manuscript.

References

[1] A. A. Velasco, C. J. Ammon, and T. Lay, "Recent large earthquakes near Cape Mendocino and in the Gorda plate: broadband source time functions, fault orientations, and rupture complexities," *Journal of Geophysical Research: Solid Earth*, vol. 99, no. B1, pp. 711–728, 1994.

[2] Y. H. Chen and Y. W. Wang, "The analysis on the deformation predition of pile-anchor retaining structure in deep foundation pit in Kunming," *Applied Mechanics and Materials*, vol. 166–169, pp. 1222–1225, 2012.

[3] C. H. Zhang and J. P. Wolf, *Dynamic Soil-Structure Interaction: Current Research in China and Switzerland*, Elsevier, Amsterdam, NY, USA, 1998.

[4] Y. G. Fang, *Theory and Application of Dynamic Interaction between Geotechnical Media and Structure*, Science Press, Beijing, China, 2005.

[5] B. K. Maheshwari, K. Z. Truman, M. H. El Naggar, and P. L. Gould, "Three-dimensional nonlinear analysis for seismic soil-pile-structure interaction," *Soil Dynamics and Earthquake Engineering*, vol. 24, no. 4, pp. 343–356, 2004.

[6] I. Takewaki and A. Kishida, "Efficient analysis of pile-group effect on seismic stiffness and strength design of buildings," *Soil Dynamics and Earthquake Engineering*, vol. 25, no. 5, pp. 355–367, 2005.

[7] H. L. Ye, Y. R. Zheng, A. H. Li, and X. L. Du, "Shaking table test study on anti-slide piles of slope under earthquake," *Chinese Journal of Geotechnical Engineering*, vol. 34, no. 2, pp. 65–71, 2012.

[8] J. Lai, Y. R. Zheng, Y. Liu, X. D. Li, and E. D. Abi, "Analysis of shaking table model test on embedded anti-slide piles under earthquake," *Electronic Journal of Geotechnical Engineering*, vol. 19, pp. 3963–3976, 2014.

[9] C. Zhang, "Analysis of the research status and trends of anti-slide pile with prestressed anchor cable," *Applied Mechanics and Materials*, vol. 638–640, pp. 338–342, 2014.

[10] X. R. Qin, "*Research on optimization design of slope reinforcement with prestressed anchor cable anti-slide piles*," M.S. thesis, China University of Geosciences, Beijing, China, 2015, 2015.

[11] X. L. Liu, Z. M. Zhang, and D. P. Zhou, "Improved calculation method of prestressed anchor cable anti-slide piles," *Journal of Rock Mechanics and Engineering*, vol. 23, no. 15, p. 2568, 2004.

[12] G. Fan, J.-j. Zhang, S.-c. Qi, and J.-b. Wu, "Dynamic response of a slope reinforced by double-row anti-sliding piles and prestressed anchor cables," *Journal of Mountain Science*, vol. 16, no. 1, pp. 226–241, 2019.

[13] J. Bi, X. Luo, H. Zhang, and H. Shen, "Stability analysis of complex rock slopes reinforced with prestressed anchor cables and anti-shear cavities," *Bulletin of Engineering Geology and the Environment*, vol. 78, no. 3, pp. 2027–2039, 2019.

[14] Z. Zou, D. Lei, G. Jiang, B. Luo, S. Chang, and C. Hou, "Experimental Study of Bridge Foundation Reinforced with Front and back rows of anti-slide piles on gravel soil slope under El Centro waves," *Applied Sciences*, vol. 10, no. 9, p. 3108, 2020.

[15] G. R. Martin and C.-Y. Chen, "Response of piles due to lateral slope movement," *Computers & Structures*, vol. 83, no. 8-9, pp. 588–598, 2005.

[16] S. K. Huang, J. Zhao, and D. Y. Liu, "Seismic response analysis of slopes supported by anti-sliding piles with prestressed anchor rods based on FLAC3D," *Earthquake Research*, vol. 39, no. 1, pp. 74–78, 2016.

[17] Y. S. Wang, G. X. Wang, Z.. Wang, and X. G. Chu, "Structural optimization of prestressed anchor anti-slide piles," *China Railway Science*, vol. 028, no. 005, pp. 11–14, 2007.

[18] A. Deng, "*Application study of multi-anchor anti-slide piles in Beijing Jietaisi landslide control project*," M.S. thesis, Academy of Railway Sciences, Beijing, China, 2007.

[19] Z. Wang, "Development and application of fully buried multi-anchor anti-slide piles," *Geotechnical Engineering*, vol. 33, no. S1, pp. 319–324, 2011.

[20] H. Ai, "*Application and optimization of slope reinforcement with anchor cable anti-slide piles in high-intensity earthquake areas*," M.S. thesis, Lanzhou Jiaotong University, Lanzhou, China, 2017.

[21] S. Feng, H. G. Wu, H. Ai, and W. Q. Feng, "Seismic optimization design and experimental study of prestressed anchor cable anti-slide piles," *Science Technology and Engineering*, vol. 18, no. 12, pp. 248–255, 2018.

[22] Z. Wu, D. Zhang, S. Wang, C. Liang, and D. Zhao, "Dynamic-response characteristics and deformation evolution of loess slopes under seismic loads," *Engineering Geology*, vol. 267, Article ID 105507, 2020.

[23] N. Ma, H. Wu, H. Ma, X. Wu, and G. Wang, "Examining dynamic soil pressures and the effectiveness of different pile structures inside reinforced slopes using shaking table tests," *Soil Dynamics and Earthquake Engineering*, vol. 116, pp. 293–303, 2019.

[24] H. Dou and P. M. Byrne, "Model studies of boundary effect on dynamic soil response," *Canadian Geotechnical Journal*, vol. 34, no. 3, pp. 460–465, 1997.

[25] N. A. Kostyukov, "Effect of the initial density of a substance on the conditions of oblique collision of shock waves," *Journal of Applied Mechanics and Technical Physics*, vol. 18, no. 3, pp. 379–384, 1978.

[26] E. S. Bruce, "Earthquake surface slip-length data is fit by constant stress drop and is useful for seismic hazard analysis," *Bulletin of the Seismological Society of America*, vol. 103, no. 2A, pp. 876–893, 2013.

[27] B. W. Xu, "*Shaking table model test of large complex structure-pile-soil,*" Ph.D. thesis, Tianjin University, Tianjin, China, 2010.

[28] M.-L. Lin and K.-L. Wang, "Seismic slope behavior in a large-scale shaking table model test," *Engineering Geology*, vol. 86, no. 2-3, pp. 118–133, 2006.

[29] R. Murugan, V. P. Raja, and P. R. Thyla, "Establishment of structural similitude for elastic models and validation of scaling laws," *KSCE Journal of Civil Engineering*, vol. 17, no. 1, pp. 139–144, 2013.

[30] J. Ferritto, "Dynamic tests of model concrete, Dynamic Modeling of Concrete Structures," vol. 73, no. 2, pp. 23–33, 1982.

[31] R. M. J. Ayres, M. T. P. Santos, P. Santos, and M. Terezinha, "Exploring similarity relations according to different contexts in mining generalized association rules," *Enterprise Information Systems*, vol. 141, pp. 137–152, 2013.

[32] A. Che, H. Yang, B. Wang, and X. Ge, "Wave propagations through jointed rock masses and their effects on the stability of slopes," *Engineering Geology*, vol. 201, pp. 45–56, 2016.

[33] I. Towhata, "Seismic wave propagation in elastic soil with continuous variation of shear modulus in the vertical direction," *Soils and Foundations*, vol. 36, no. 1, pp. 61–72, 1996.

[34] C. Simone and G. Francesco, "Full waveform seismological advances for micro seismic monitoring," *Advances in Geophysics*, vol. 56, no. 12, pp. 169–228, 2014.

[35] J. L. Fu, "*Research on the characteristics of EPS shock-proof packaging materials with different structures*," M.S. thesis, Hunan University, Hunan, China, 1990.

[36] Z. Hellwig, "The transitivity of the correlation relation of random variables and some econometric implications obtained therefrom," *Przegld Statyst*, vol. 23, no. 1, pp. 3–20, 1976.

[37] Z. F. Liu and P. S. Shen, "Quasi-velocity spectrum estimation of total input energy spectrum," *Engineering Aseismic and Reinforcement Reconstruction*, vol. 30, no. 2, pp. 20–32, 2008.

[38] J. W. Baker and C. A. Cornell, "Correlation of response spectral values for multicomponent ground motions," *Bulletin of the Seismological Society of America*, vol. 96, no. 1, pp. 215–227, 2006.

[39] E. T. Wall, "The generation of Liapunov functions in control theory by an energy metric algorithm," *Joint Automatic Control*, vol. 20, no. 9, pp. 172–179, 1968.